Journal of Operation and Automation in Power Engineering

Vol. 14, No. 3, Aug. 2026, Pages: 209-221

http://joape.uma.ac.ir

Research Paper

Designing a Multi-Objective Optimized Parallel Process Controller for Frequency Stabilization in an Islanded Microgrid

Hossein Shayeghi *, *Alireza Rahnama* , and *Hamed Mojarad*

Energy Management Research Center, University of Mohaghegh Ardabili, Ardabil, Iran.

Abstract— *Load-frequency control plays a critical role in maintaining the stability and reliability of islanded microgrids, where the absence of a large interconnected grid makes frequency regulation more challenging. With the increasing integration of renewable energy sources and energy storage systems, the stochastic and uncertain nature of μGs component's behavior has amplified the need for advanced LFC mechanisms, making it a focal area of research for decades. This paper introduces a novel parallel process FOPI–FPOD controller optimized for robust LFC and stability in μGs. Employing time and frequency domain objective costs, a multi-objective particle swarm optimization algorithm with nonlinear time-varying coefficients generates a Pareto front, with fuzzy decision-making selecting optimal designs. The proposed controller demonstrates strong robustness by effectively handling uncertainties such as sudden load changes, RES fluctuations, and parametric variations, while maintaining stable frequency regulation. The controller's performance is evaluated under four scenarios: sudden load changes with time delays, uncertainties in RESs, parametric system uncertainties, and energy storage systems' impact. Comparative analysis with PID, FOPID, and PD(1+PI) controllers demonstrates the proposed design's superior stability and resilience, providing a robust solution for frequency stabilization in μGs. Numerical results demonstrate that the proposed FOPI–FOPD controller significantly outperforms traditional methods, achieving lower error indices, reduced frequency deviations, and more efficient utilization of energy storage systems under various scenarios and energy storage systems participation levels. These findings highlight its robust and adaptive performance in ensuring stable and efficient LFC task for an islanded μGs control.*

Keywords—Fractional order controller, load-frequency control, multi-objective optimization, microgrid control.

NOMENCLATURE

Abbreviations

μG	Microgrid
DEG	Diesel engine generator
ESS	Energy storage system
FC	Fuel cell
FDM	Fuzzy decision-making
FO	Fractional order
GM	Gain margin
IAE	Integral of absolute error
IO	Integer order
ISE	Integral of square error
ITAE	Integral of time-weighted absolute error
ITSE	Integral of time-weighted square error
LFC	Load-frequency control
OC	Objective cost
PID	Proportional-derivative-integral
PM	Phase margin
PSO	Particle swarm optimization
RES	Renewable energy sources
SSE	Steady-state error
TF	Transfer function
WTG	Wind turbine generator

Symbols

Δf	Frequency deviation
ΔP_L	Load disturbance
$\Delta f_{\max}$	Maximum frequency deviation
$\Delta f_{Threshold}$	The minimum frequency deviation for responsive loads excitation
τ	Control signal time delay
ζ	Minimum damping value of the system's poles
c_1, C_2	Self and global learning coefficients
c_{1i}, C_{1f}	Self-learning coefficient initial and final values, respectively
c_{2i}, C_{1f}	Social-learning coefficient initial and final values, respectively
It	Optimization algorithm counter
It_{max}	Maximum number of optimization algorithm execution
K_P, K_I, K_D, K_T	Proportional, integral, derivative, and tilt control operators' coefficients, respectively
K_v, T_v	Governor's gain and time constant
K_{PV}, T_{PV}	Photovoltaic unit's gain and time constant
K_{WTG}, T_{WTG}	WTG unit's gain and time constant
M, D	System inertia and damping coefficients, respectively
N	Derivative filter coefficient
T_t, T_g	Diesel generator's turbine and governor time constant, respectively
t_{sim}	Simulation time
U	Controller output signal
U_1, U_2	Proposed controller's internal control signals

Received: 23 Nov. 2024
Revised: 08 Feb. 2025
Accepted: 08 Feb. 2025
*Corresponding author:
E-mail: hshayeghi@gmail.com (H. Shayeghi)
DOI: 10.22098/joape.2025.16246.2255

V_{cut-in}, $V_{cut-out}$, V_{rated} Wind turbine's cut-in, cut-out, and rated speed, respectively

w Inertia factor

1. INTRODUCTION

The increasing complexity of modern power systems, particularly with the integration of renewable energy sources (RES), demands innovative solutions for efficient and stable operation. In this regard, load-frequency control (LFC) plays a pivotal role in ensuring system stability and reliability. This section will outline the importance of the LFC in modern power systems and emphasize the relevance of this research in addressing current challenges.

1.1. The importance of the subject

An imbalance in the system's generation-consumption process might cause improper tripping of system protection. Moreover, an extreme variation in system frequency can result in substantial harm to a wide range of equipment in the generating, distribution, and consumer sectors. System blackouts may occur if the load frequency control (LFC) mechanism fails to operate correctly and regularly [1]. This highlights the significance of employing effective control techniques specifically tailored for LFC loops. The control systems should be structured to promptly fix the imbalance, since any delay might lead to extensive blackouts due to the cascading effects of the problem [2].

The stability, reaction time, and capacity to maintain frequency within acceptable limits despite disruptions are strongly impacted by the optimal parameter values in LFC of a μG. Inadequate tuning of the parameters in LFC can lead to instability in the μG, resulting in possible oscillations or divergence in frequency. This instability poses a risk of equipment damage. The system's dynamic responsiveness may be disrupted, resulting in either sluggish or too aggressive reactions to disturbances, which can cause protracted frequency deviations. In addition, inadequate tuning can lead to more severe oscillations and diminished system resilience, rendering it more susceptible to shocks and load variations. These problems might lead to increased energy expenses and reduced overall reliability and efficiency of the μG.

Ensuring a sufficient electrical power reserve to swiftly attain a balance between generation and consumption is of utmost importance, considering that RESs comprise a significant portion of modern μG's power generating share. The problem of inadequate reserve undoubtedly has a profound effect on the stability of power systems. On one side, there is a continuous increase in the demand for electric power, and the development of conventional electricity generation units or power distribution networks is complex in several ways. However, despite their positive qualities, renewable energy sources (RESs) are insufficient for reserving power demand because of their restricted capacity and intermittent nature [3].

1.2. Literature review

Power system experts have long debated the LFC problem and the best controller architecture to use as a supplementary controller [1]. Primarily, it is necessary to build a suitable control mechanism due to the introduction of novel systems that provide unique difficulties. Furthermore, it is crucial to consistently strive for enhancing the quality of electrical services provided in order to guarantee the secure functioning of electrical appliances and prevent disappointment among consumers. Scientists have employed many methods to enhance the system's capacity to adapt and react effectively to disruptions and anticipated operating circumstances. A common method in this discipline involves developing and enhancing new controllers [1].

Due of their simplicity and typically good performance, classic controllers such as proportional-integral-derivative (PID) are extensively utilized in the LFC domain [4]. When dealing with complicated systems, nonlinearities in the system, or uncertainties, however, research has revealed that the PID controller becomes less effective [5]. Its operation is also demonstrated to be rather sensitive to the operating point and parameters of the system. The FO operators have partially but not completely moderated these problems [6].

Other control techniques, in addition to classical controllers, have been explored for the LFC purposes of the power systems. For instance, the H-infinity technique produces a modest control signal, but its effectiveness is directly influenced by the system's mathematical model, which contains a number of uncertainty factors [7]. The model predictive control (MPC) method, which is sensitive to the system parameters like the H-infinity technique, has a good performance in dealing with multivariable processes [8, 9]. The sliding-mode controllers (SMC) perform better against parametric uncertainty in the investigated model, and the problem dimensions are adequate for designing an appropriate control mechanism to accomplish the LFC objective; nevertheless, the dynamic responses of the system using the SMC suffer from chattering [10, 11]. Frequency stability is achieved in a conventional hybrid power system by employing a control approach that combines FO operators in a fuzzy cascade control structure [12]. While this control method has helped researchers in obtaining good results, the optimality of membership functions and fuzzy rule bases has not been investigated. The impact of non-linear elements and the controller's effectiveness as a practical tool are also in question. Generally, Adaptive fuzzy controllers perform well at broad working points and in non-linear systems, but their correctness depends on the membership functions and fuzzy rule bases [13, 14]. Learning-based approaches that are simple to incorporate into various systems depend on the caliber of the training data [15]. According to the literature, master-slave controllers have also performed well in the LFC objectives [16]. The extra control loop present in this class of controllers, however, makes it difficult and complex to build and tune them.

Evaluating the prior control approaches reveals that, in addition to their benefits, they all have inherent drawbacks. Different approaches are taken to address the controllers' challenges [1]. For a two-area hybrid power system model with hydro, thermal, gas, and wind power plants, Hakimuddin *et al.* looked into the optimal design and implementation of a PI structured optimal LFC controller using full state vector feedback control theory [17]. One of the frequent approaches is to alter the common controllers' configuration to enhance their performance in desired control purposes [18, 19]. The cascade type of the PID controller is offered in the form of PD(1+PI) and has been employed for a different purpose, including the LFC of the μGs, and has consistently outperformed its classical predecessor [20, 21]. For LFC in conventional power systems, the (1+PD)-PID cascaded controller is utilized. However, the authors do not account for the renewable energy sources that have considerable swings in their output, and the studied system is entirely linear [22]. The TDF(1+FOPI) controller is introduced by altering integer order (IO) operators of the cascaded PID controller to their FO type [23]. Results show that if the controller is properly adjusted, FO actions provide the design a greater degree of freedom, enabling better dynamic responses to be recorded. To maintain the stability of a multi- μG system, Singh and Arya have introduced the ITDF controller [24]. The developed controller is supplemented with a second control cycle as part of the proposed control mechanism. A two-zone μG has been employed to test the proposed design and compare its time- and frequency-domain performance to that of PID and IPD controllers. In general, the issues with classical controllers can be addressed and their effectiveness can be enhanced by reconfiguring conventional controllers and using the FO control actions. Obviously, it should be emphasized that the new configurations should be developed in such a way that improving performance does not come at the expense of adding so more optimization variables and creating new challenges [25].

A complex optimization problem must be solved in order to design an optimal controller for the LFC. Time-domain OC, such as the Integral of the Absolute Error (IAE) and the Integral of the Time-weighted Absolute Error (ITAE), emphasize transient response attributes, including the minimization of overshoot, the reduction of settling time, and the facilitation of swift recovery following disturbances. These functions facilitate the rapid restoration of the system to a stable condition following a frequency deviation. On the other hand, frequency-domain OCs, such as minimizing gain and phase margins, adhering to certain bandwidth limitations, or optimizing pole placements, assess the resilience and stability of the system against a broad spectrum of disturbances across various frequencies. They assist in configuring the frequency response to mitigate resonance challenges, enhance disturbance rejection, and guarantee robust performance amid parameter uncertainties. By optimizing both domains, the controller may achieve a rapid and steady recovery in the time-domain while ensuring strong, disturbance-resistant performance in the frequency-domain, resulting in a more resilient and reliable load-frequency management system in μGs.

If the appropriate solution method is employed, the global optimum and the best parameter values for the controller can be determined. Various techniques have been used for this purpose [19]. The optimum tuning of the PID controller with cascade and parallel structure is performed using the particle swarm optimization (PSO) approach with time-varying acceleration coefficients. According to the findings, this version of the PSO algorithm has a higher probability of finding global optimum solutions and a quicker convergence rate [26]. In [27], the authors optimize the IPD-(1+I) multilevel controller using the sine-cosine technique. The Bonobo optimization (BO) algorithm is utilized to well-tune the FO cascade TDF(1+FOPI) controller [23]. To regulate the frequency of a two-zone μG, Peddakapu *et al.* have developed the CFOID-FOPIDN cascade controller (cascade combination of fractional order-based integral derivative and proportional integral derivative with filter) , which uses the Barnacle mating optimizer algorithm to optimize its coefficients [19]. The hybrid gravitational-firefly algorithm has been used to optimally adjust the PI controller in a two-area power system [28]. Gupta *et al.* have introduced and used an intelligent hybrid optimization algorithm for PID controller design in a traditional multi-source power system [29].

Generally, utilizing demand-side management capabilities to fast switch between off and on states has resulted in rapid responses. This has subsequently decreased conventional power generating units' mechanical and thermal stress [30]. Different methods have been tried and utilized in the field of the DSM, but RLs are a popular method of bolstering the control loop in LFC issues. A fuzzy controller is used for the LFC control loop in [31], where the implementation of the EVs model as support for the control loop is investigated considering a control law for the RLs aggregator excitation range. By looking at [32], we can see that researchers have investigated how effectively to get RLs involved in adjusting μG frequency. Different studies have shown that using the capacity of RLs improves the dynamic stability of μGs and makes it faster and easier to address disturbances [5, 32].

1.3. Research gaps and paper contributions

Because new problems arise with modern systems, controller design strategies should reflect these circumstances [1]. Based on the goals and dynamics of the target system, the optimization problem and OC should be appropriately defined. In this regard, recent studies have defined the optimization problem in general, rather than according to the investigated system, despite the introduction of control mechanisms with appropriate performance [19, 24].

Time delays in current μG structures are most commonly caused by data loss or communication line saturation [33]. Many recent studies have not considered the impact of these factors in the design and evaluation of their proposed control strategies. The mentioned topics, along with the need to design simple, efficient control mechanisms with high-speed response, are the topics that are considered as study gaps in this article.

The main objective of this study is to design a robust and adaptive parallel process controller for frequency stabilization in islanded μGs, addressing the challenges posed by the integration of renewable energy sources (RES) and energy storage systems (ESS). In islanded microgrids, frequency stabilization is more challenging due to the lack of support from the main grid, requiring robust and adaptive controllers. In contrast, grid-connected microgrids benefit from the main grid's stability support, but the proposed controller can still enhance the dynamic response of DERs and ensure seamless mode transitions. While existing controllers, such as PID and FOPID, have been widely used, they often struggle to handle the stochastic and uncertain nature of modern μGs. This work introduces a novel FOPI–FOPD nested controller optimized using a multi-objective PSO algorithm with non-linear time-varying acceleration coefficients (NTVAC). The proposed controller not only improves frequency stability but also demonstrates superior performance under various uncertainties, including sudden load changes, RES fluctuations, and parametric variations. By addressing these critical gaps, this study provides a significant contribution to the field of load-frequency control in islanded μGs.

Briefly, this paper's objectives can be summed up as follows:

- To design a novel parallel process FOPI–FOPD controller for optimal μG LFC and system stability establishment,
- To define time and frequency domain objective functions for the purpose of optimizing controllers to maintain μG stability, and tuning the controller by solving a multi-objective problem,
- To compare the performance of the proposed control mechanism by comparing the best setting of conventional and common controllers with the proposed controller.

2. THE MODEL OF THE SYSTEM UNDER STUDY

Studies on LFC in μGs frequently utilize dynamic models in the frequency domain. μG dynamic models generally possess a high level of complexity [34]. Frequency studies and analyses commonly employ linearized system models, even though μGs inherently consist of components and elements with nonlinear and time-varying characteristics. Multiple investigations have shown that the results of hardware testing align well with lower-order linear models [35]. Therefore, these models are considered suitable for use in simulations. The general scheme of the system is illustrated in Fig. 1, and the simplified dynamic models of various units were employed in this section. While the detailed model in Fig. 1 captures the full complexity of the μG, the linearized model in Fig. 1 provides a simplified representation that is more amenable to control analysis and design. Both models are used in this study to ensure a comprehensive understanding of the system's behavior. This model is further detailed in [29]. This system utilizes a combination of diesel generators (DEG), solar photovoltaic units (PV), and wind turbines (WTG) as sources of power generation. The system's storage devices encompass the fuel cell (FC), and battery (BESS). Renewable energy-based generation sources typically do not participate in Load Frequency Control (LFC) loops due to their output capacity being reliant on weather conditions and the uncontrollable nature of this dependency.

2.1. Units' dynamic model

It is important to first highlight the critical role of each individual unit within the overall μG framework. The dynamic models of various components, including the diesel generator (DEG), wind turbine generator (WTG), photovoltaic (PV) unit, fuel cell (FC) and aqua-electrolyzer (AE), battery storage system (BESS), and load-inertia system, are essential for understanding the

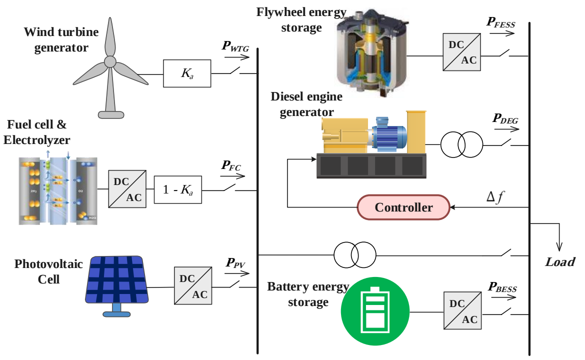

Fig. 1. General scheme of the under-study μG.

interdependencies and behaviors that define the system's operation. These models incorporate key physical characteristics and control mechanisms that govern the performance of each unit under various operating conditions. The models used in this study are based on validated references and account for practical limitations [14, 35]. The following subsections will detail these dynamic models, with an emphasis on their formulation, the assumptions made during modeling, and their relevance to the broader system dynamics. The constant values used in this model are adopted from [1, 14], which provides validated parameters for similar systems.

A) *Diesel engine generator*

Turbine and governor systems are integral components in both diesel generators and thermal turbogenerators. Within a certain frequency disturbance range, fixed speed variations do not impact the position of the diesel generator's governor valve, resulting in the governor remaining inactive. This phenomenon is referred to as the governor's dead band. The resulting oscillatory response can be approximated by a sinusoidal function with a period of 2 seconds. The block diagram representing the governor, including the effects of the dead band for the diesel generator, can be modeled as Fig. 2-(a) [36]. Additionally, in practical applications, the generator's production rate is subject to certain limitations. Research indicates that the generation rate constraint (GRC) significantly impacts the system's dynamic performance, particularly in terms of overshoot and undershoot. Consequently, the block diagram of the transfer function associated with the turbine can be represented as Fig. 2-(b) [37].

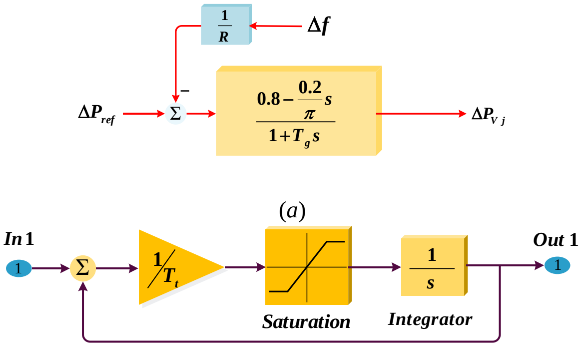

(*a*)

(*b*)

Fig. 2. Diesel engine generator model. (a) Governor dead-band model, (b) Generation rate constraint model.

B) *Wind turbine generator*

The output power of a WTG is directly influenced by wind speed. If the wind speed falls below the cut-in speed (V_{cut-in}), the turbine cannot generate electricity. Conversely, when the wind speed exceeds the cut-out limit ($V_{cut-out}$), the turbine shuts down to prevent damage, resulting in zero power generation. In the Fig. 3, the relationship between the wind turbine's output power and varying wind speeds is illustrated. Furthermore, a first-order transfer function can be employed to characterize the dynamic response model of the wind turbine, as demonstrated in Eq. (1) [38].

$$\Delta P_{WTG} = \left(\frac{K_{WTG}}{1 + sT_{WTG}} \right) \Delta P_{wind} \tag{1}$$

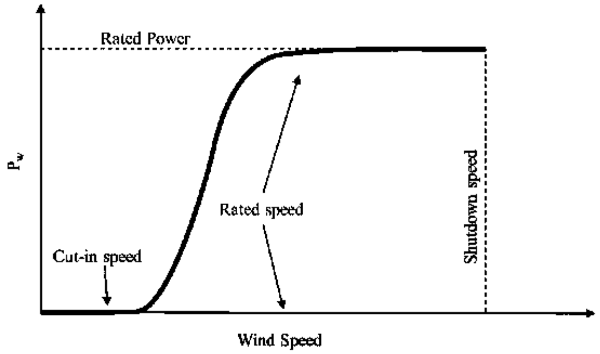

Fig. 3. General power output curve of a wind turbine as a function of varying wind speeds, illustrating key operational regions including cut-in, rated, and cut-out wind speeds.

C) *Photovoltaic unit model*

Solar energy is the most abundant energy source globally; however, its direct utilization remains relatively low. The output power of a solar cell, along with its linear model, is outlined as follows [39]:

$$P_{pv}^{irradiation} = \eta S \Phi \left\{ 1 - 0.005 \left(T_a + 25 \right) \right\} \tag{2}$$

$$\frac{\Delta P_{pv}}{\Delta \Phi} = \frac{K_{pv}}{1 + sT_{PV}} \tag{3}$$

In this context, ϕ represents the solar irradiance in KW/m^2, while η denotes the efficiency of the solar cell, typically ranging from 9% to 12%. Additionally, S refers to the surface area of the PV cell in m^2. In Eq. (3), K_{pv} and T_{pv} represent the coefficient and time constant of the solar cell's transfer function, respectively.

D) *Fuel cell and aqua-electrolyzer units*

In the analyzed μG, it is assumed that a segment of the power produced by the WTG is employed to satisfy the energy demands of the AE for hydrogen production. The first-order frequency models for both the FC and the AE are provided below.

$$\frac{\Delta P_{FC}}{\Delta P_{AE}} = \frac{K_{FC}}{1 + s\,T_{FC}} \tag{4}$$

$$\frac{\Delta P_{AE}}{\Delta P_{WTG} \left(1 - K_n \right)} = \frac{K_{AE}}{1 + s\,T_{AE}} \tag{5}$$

In the equations presented above, K_{FC} and T_{FC} denote the coefficient and time constant of the fuel cell's transfer function, respectively, while K_{AE} and T_{AE} represent the coefficient and time constant of the electrolyzer's transfer function. Additionally, in Eq. (5), $1 - K_n$ signifies the proportion of the wind turbine's generated power allocated to the electrolyzer for hydrogen production.

E) Battery energy storage systems

μGs may be unable to provide sufficient power to their consumers when wind and solar energy resources are insufficient. Effectively addressing these vulnerabilities is critical for ensuring the system's stability and reliability. To mitigate this issue, BESS are integrated into the system. The linearized transfer function model of the battery energy storage system can be represented as follows.

$$P_{BESS} = \frac{K_{BESS}}{1 + T_{BESS}s} \tag{6}$$

F) Load-inertia dynamic model

In essence, the stability of a power generation and distribution system refers to the effective balance between the total generated power and the system's load requirements. This balance is maintained based on the difference between the reference power demand, P_g^*, and the actual generated power P_g, as described by the following equation:

$$\Delta P_g = P_g^* - P_g \tag{7}$$

The transfer function that characterizes system frequency alterations in relation to per-unit frequency deviation, considering the time delays in frequency variations and power deviations, is defined as follows:

$$\Delta P_{\mu G} = \frac{\Delta f}{\Delta P_g} = \frac{1}{Ms + D} \tag{8}$$

Where, the parameters M and D are the inertia constant and the damping constant, respectively.

3. PROPOSED CONTROL STRATEGY: FOPI–FOPD NESTED CONTROLLER

The proposed controller design involves modifying the configuration of traditional controllers by substituting their input-output control operators with FO elements, thereby providing the designer with enhanced flexibility and a greater degree of freedom. In multi-tier controller architectures, the control signal at the output of one tier serves as the input for the subsequent tier. This research design proposes a parallel and nested structure, specifically FOPI–FOPD, to address the limitations of traditional and conventional controllers. The controller comprises two components configured in parallel, FOPI and FOPD, and the output signal is derived from the difference between these two outputs. The proposed FOPI–FOPD nested controller acts as a process controller, dynamically managing the power generation and load variations within the μG to ensure frequency stability.

Finally, the transfer function of the proposed controller will be as given by Eq. (9). Also, Fig. 4 shows the schematic structure of this controller.

$$\frac{\Delta U_c}{\Delta f} = \underbrace{\left(K_{P1} + \frac{K_I}{s^{\alpha}}\right)}_{FOPI} - \underbrace{\left(K_{P2} + K_D \frac{s^{\beta} N}{N + s^{\beta}}\right)}_{FOPD} \tag{9}$$

The proposed controller structure encompasses three primary features:

- The implementation of a nested architecture that facilitates the concurrent operation of two FOPI and FOPD controllers in parallel;
- The incorporation of a derivative filter to enhance stability and mitigate noise;
- The utilization of FO operators in lieu of IO types, thereby augmenting design flexibility and optimizing outputs.

The subsequent section elucidates the proposed methodology for the optimal tuning of the controller parameters.

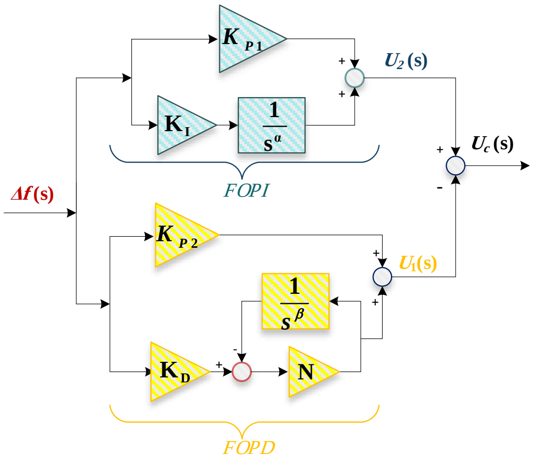

Fig. 4. Proposed FOPI–FOPD controller scheme.

4. OPTIMIZATION PROBLEM AND SOLUTION METHOD

Even the most resilient control systems cannot function optimally if they are not adequately calibrated. In the context of the LFC, suboptimal tuning of the controller will yield an inadequate dynamic response, leading to increased energy costs or outages. In this section, an appropriate OC to optimize the controller's parameters is established in alignment with the system's dynamic objectives, followed by a discussion of the strategy to address this optimization problem.

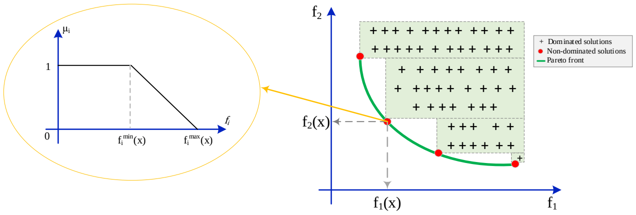

Fig. 5. Membership functions of the fuzzy objective functions used to evaluate and select the best compromise solution from the Pareto optimal set.

4.1. Objective cost

In formulating the system's objective cost (OC), it is essential to account for considerable uncertainty arising from modeling approximations and other stochastic disturbances, alongside variations in system load; thus, the frequency domain technique is incorporated into the optimization OC. Unlike a standard objective function, the term 'cost' emphasizes the potential consequences of suboptimal controller tuning, such as increased energy losses or compromised system stability. The OC is designed to minimize these undesirable outcomes while ensuring optimal performance under various operating conditions. To this end, alongside the primary objective function obj_1, which is articulated in the time domain and predicated on the integral of the error magnitude weighted by time t, the secondary OC obj_2 is delineated in the frequency domain. The obj_2 is formulated to ensure that the poles of the closed-loop system are positioned to the left of a specified vertical line in the complex plane.

$$obj_1 = \int_0^{t_{sim}} t\,|\Delta f|\,\mathrm{d}t \tag{10}$$

Table 1. Optimal parameters of controllers after optimization.

Controller	Parameters
FOPI–FOPD	$K_{P1} = 10.9690,\ K_{P2} = 0.0803,\ K_D = 1.9654,\ \alpha = 0.0502,\ K_I = 30.0781,\ \lambda = 1.0085,\ N = 3275$
PD(1+PI)	$K_P = 3.4836,\ K_I = 2.1211,\ K_D = 0.0028,\ K_{PP} = 0.5358$
FOPID	$K_P = 19.9891,\ K_I = 19.9091,\ \lambda = 1.003,\ K_D = 6.4075,\ \mu = 0.9894$
PIDn	$K_P = 0.9922,\ K_I = 1.0040,\ K_D = 1.0521,\ N = 923$

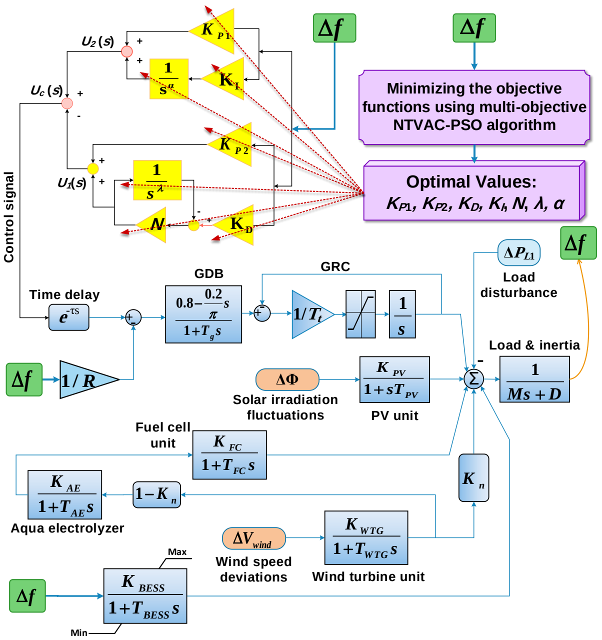

Fig. 6. General scheme of the optimization process and block system's block diagram.

Table 2. System gain and phase margin values with optimized controllers.

Controller	GM	GM's phase $\omega_{c_{gm}}$	PM	PM's phase
FOPID	1.6070	6.4250	Inf	Nan
PIDn	1.2619	7.7054	Inf	Nan
PD(1+PI)	1.3915	6.4754	38.7916	3.0372
FOPI–FOPD	1.6452	6.2059	Inf	Nan

$$obj_2 = \sum_{i=1}^{N_p} \max\left\{\operatorname{Re}(\lambda_i) - \min\left\{-\zeta\left|\operatorname{Im}(\lambda_i)\right|, \gamma\right\}\right\} \tag{11}$$

In Eq. (10), t_{sim} denotes the simulation duration. In Eq. (11), λ_i denotes the $i-th$ pole of the closed-loop system, while ζ signifies the minimum damping value of the $i-th$ pole. The value of γ is established at 0.23, derived from empirical observations of the system under investigation across various operating conditions. Also, in Eq. (11), λ_i is used as a tuning parameter to balance the trade-offs between different objectives in the multi-objective optimization process. While λ varies during the optimization to generate the Pareto front, the focus of this study is on the final Pareto-optimal solutions rather than the intermediate values of λ. This approach allows us to evaluate the controller's performance across various operating scenarios without being constrained by specific optimization trajectories.

The range of controller coefficients is bounded by Eq. (12) which represents the search space of the optimization problem. If K represents a controller parameter, then we have:

$$K^{\min} \leq K \leq K^{\max} \tag{12}$$

Table 3. Assumptions related to different scenarios in the study.

Scenario	Load disturbances ΔP_L	RESs' fluctuations	Time delay (τ)	Parametric uncertainties
1	✓		20 ms	
2	✓	✓	40 ms	
3	✓		20 ms	✓
4	✓	✓	20 ms	✓

Table 4. Time domain evaluation indices for the dynamic response of the system in the first scenario.

Controller	Index					
	ISE $\times 10^3$	ITSE $\times 10^3$	IAE $\times 10^2$	ITAE $\times 10^2$	Max $\lvert\Delta f\rvert$ (Hz)	Total ΔP_{ESS} (p.u)
FOPID	0.7300	24.7200	11.9410	417.8299	0.01534	0.2862
PIDn	0.7900	26.1600	14.3801	498.5589	0.01523	0.3444
PD(1+PI)	0.6100	18.4222	12.3890	384.6971	0.01531	0.2961
FOPI–FOPD	0.4900	15.0700	9.1140	273.5060	0.01500	0.2198

For the proposed FOPI–FOPD controller, constraint Eq. (13) must hold for all Ks belonging to the set $\{K_{P1},\ KI,\ \alpha,\ K_{P2},\ K_D,\ \beta\}$.

4.2. NTVAC-PSO algorithm

The PSO algorithm is a nature-inspired optimization technique based on the social behavior of bird and fish schools [37]. Consequently, PSO emulates the collective behavior of individuals. In the PSO, an initial population of particles is established, and the members of this population navigate the problem space at specific velocities. The velocities are randomly modified in each iteration based on the optimal experiences of individual particles and the superior recollections of others. The particle movements within the problem space ultimately converge towards an optimal or near-optimal solution.

Particle i's position at iteration t is represented by a vector $x_i \in R^n$. Iteratively, all particles accelerate to their next position using their velocity vector, $v_i \in R^n$ for the $i-th$ particle as below:

$$x_i(t) = x_i(t-1) + v_i(t) \tag{13}$$

The velocity vector in Eq. (13) is determined by individual and neighbor experience. The particle's past decisions determine the first factor. Imagine a decision (relocating) solved a problem better than before. It succeeds and updates the particle's best memory (p_{best}). Neighborhood knowledge, or social knowledge, is the second velocity vector factor and can be collective or local. Each iteration through all particle positions, collective experience attracts particle i to the global best (g_{best}). Note that the best position yields the optimal OC value at each iteration. The PSO is a social behavior algorithm because particles in a population must interact to find optimal solutions. Iteration i's particle velocity vector is:

$$\begin{aligned} v_i(t) = w\, v_i(t-1) + c_1 rand_1(0,1)\,(p_i - x_i(t-1)) + \\ c_2 rand_2(0,1)\,(p_g - x_i(t-1)) \end{aligned} \tag{14}$$

Personal experience and social knowledge affect the particle's movements as acceleration coefficients c_1 and c_2 in Eq. (14). Two random coefficients change self and global experience contributions. The random coefficients $rand_1$ and $rand_2$ are uniformly distributed in [0,1].

The optimal adjustment of the PSO coefficients has been studied extensively because of their impact on algorithm performance.

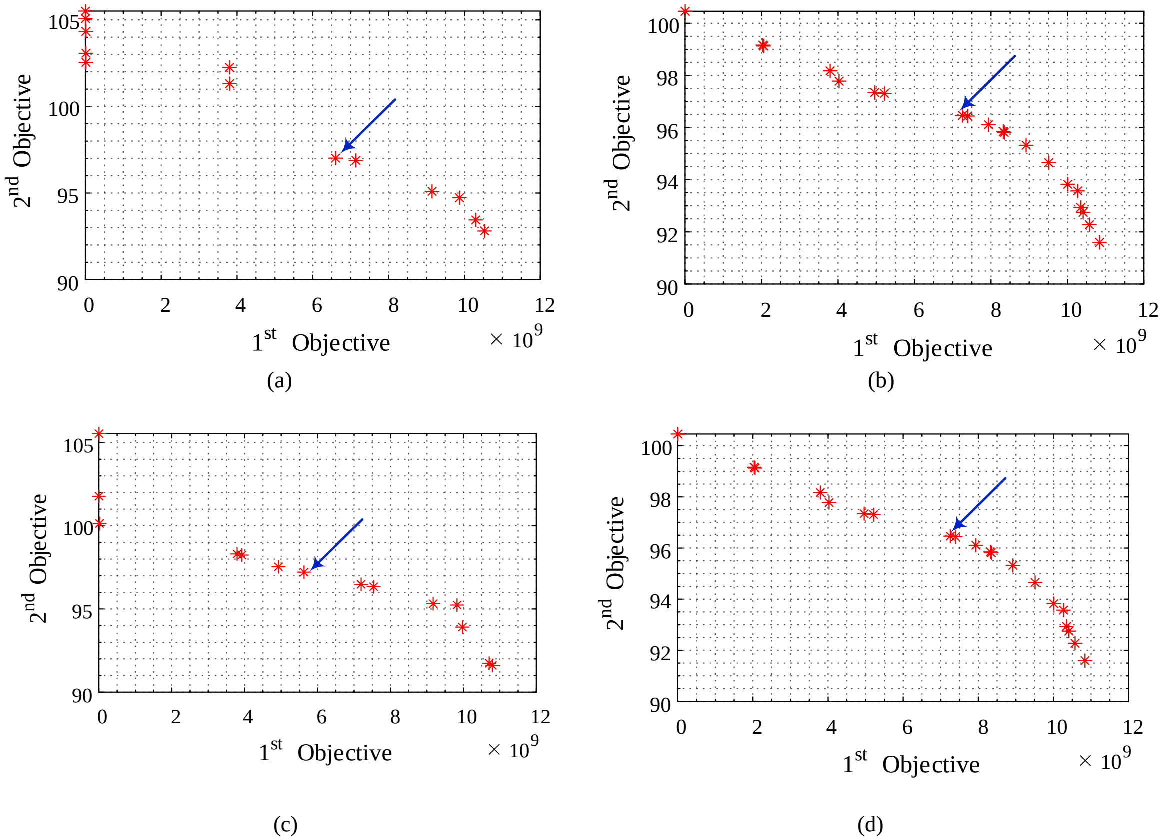

Fig. 7. Pareto front curve for TVAC-MOPSO optimization algorithm with (a) PID, (b) PD(1+PI), (c) FOPID and (d) FOPI–FOPD controllers. Optimal response in fuzzy method is shown by arrow sign on the Pareto front graphs.

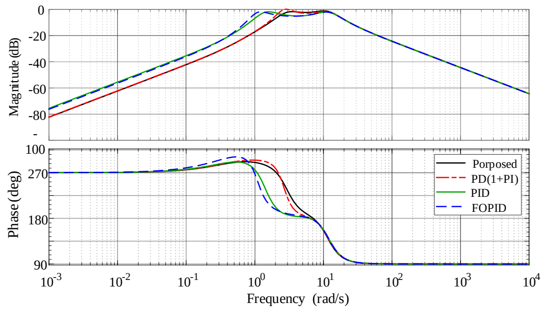

Fig. 8. The Bode diagram of the studied system with optimized controllers.

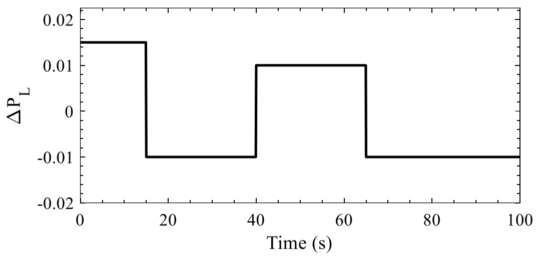

Fig. 9. Load disturbances applied on the demand side for the first scenario in (p.u).

Table 5. Time domain evaluation indices for the dynamic response of the system in the second scenario.

Controller	Index					
	ISE $\times 10^5$	ITSE $\times 10^3$	IAE $\times 10^2$	ITAE	Max $\lvert\Delta f\rvert$ (Hz)	Total ΔP_{ESS} (p.u)
FOPID	17.1698	7.8999	8.2989	4.0113	0.0050	0.1944
PIDn	18.3151	8.5989	9.1459	4.4415	0.0049	0.2168
PD(1+PI)	7.8635	3.3555	6.2245	3.2442	0.0050	0.1455
FOPI–FOPD	**7.1214**	**2.8999**	**5.1799**	**2.5609**	**0.0048**	**0.1214**

To search every corner of the search space, the NTVAC-PSO algorithm balances individual learning coefficient changes and social knowledge. From the start of the algorithm to the end, individuals should rely less on individual experience and more on collective experience. Thus, changing acceleration coefficients can be nonlinear as below. The parameters for the NTVAC-PSO algorithm, including c_{1i}, c_{1f}, c_{2i}, and c_{2f}, are selected based on [5], ensuring optimal performance.

$$c_1 = (c_{1i} - c_{1f}) \exp\left[-(4it/it_{\max})^2\right] + c_{1f} \tag{15}$$

$$c_2 = (c_{2i} - c_{2f}) \exp\left[-(4it/it_{\max})^2\right] + c_{2f} \tag{16}$$

The NTVAC-PSO, which serves as the foundation for the problem-solving approach in this study, is briefly summarized here. For a more detailed explanation, readers are referred to [5]. The algorithm is adapted to optimize the proposed controller parameters, ensuring robust performance under dynamic conditions.

4.3. Non-dominant sort

The NDS method creates Pareto front ranks and divides solutions into fronts with different ranks. After ignoring the classified individual group, another layer of non-dominated population members is considered [29]. In the initial sorting, each

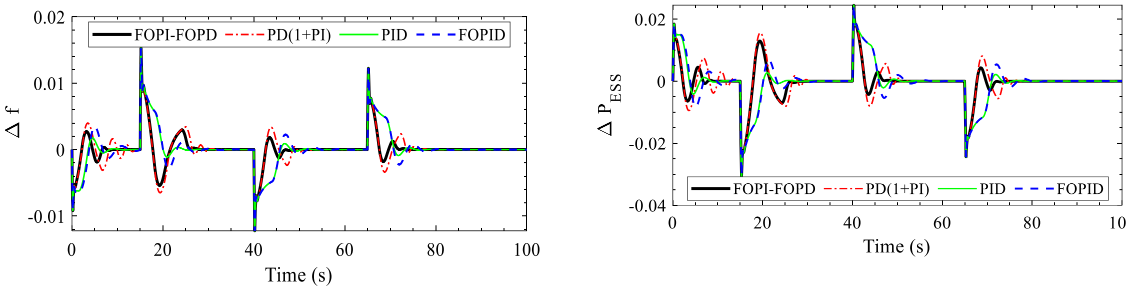

(*a*) (*b*)

Fig. 10. Dynamic response of the system in scenario 1. (a) System frequency fluctuations (Hz), (b) Output variations of BESS and FC storages (p.u). Solid line: FOPI–FOPD, dashed line: PID, dotted line: PD(1+PI) and dash-dotted line: FOPID.

Table 6. Time domain evaluation indices for system dynamic response in the third scenario.

Parameter	**Controller**	**Index**					
		ISE $\times 10^5$	**ITSE $\times 10^5$**	**IAE $\times 10^2$**	**ITAE $\times 10^2$**	**Max $\|\Delta f\|$ (Hz)**	**Total ΔP_{ESS} (p.u)**
D=0.25D$_0$, H=0.25H$_0$	**FOPID**	2.9176	1.7535	0.7900	1.0102	0.0110	0.0188
	PIDn	6.5619	10.2190	1.6679	3.5990	0.0110	0.0401
	PD(1+PI)	7.2204	13.5760	2.0590	6.4000	0.0110	0.0494
	FOPI–FOPD	**2.6748**	**1.3581**	**0.6700**	**0.6600**	**0.0110**	**0.0162**
D=0.5D$_0$, H=1.5H$_0$	**FOPID**	2.9167	3.5158	1.1110	2.6409	0.0053	0.0263
	PIDn	6.2309	11.3840	1.7658	4.2889	0.0053	0.0421
	PD(1+PI)	7.0622	15.9878	2.2222	7.8298	**0.0053**	**0.0531**
	FOPI–FOPD	**2.2618**	**1.5742**	**0.6700**	**0.7100**	**0.0053**	**0.0162**
D=1.25D$_0$, H=2.0H$_0$	**FOPID**	3.0956	4.7289	1.2789	3.9679	0.0048	0.0304
	PIDn	6.2370	11.9578	1.7990	4.7098	0.0048	0.0432
	PD(1+PI)	7.1471	17.2134	2.2990	8.6109	0.0048	0.0549
	FOPI–FOPD	**2.2840**	**1.7747**	**0.7100**	**0.8799**	**0.0048**	**0.0710**

Table 7. Time domain evaluation indices for system dynamic response in the fourth scenario.

$\boldsymbol{\Delta P_{ESS}^{\max}}$	**Controller**	**Index**					
		ISE $\times 10^5$	**ITSE $\times 10^3$**	**IAE $\times 10^2$**	**ITAE $\times 10^2$**	**Max $\|\Delta f\|$ (Hz)**	**Total ΔP_{ESS} (p.u)**
0.5 $\boldsymbol{\Delta P_{ESS}^{\max,ini}}$	FOPID	14.4999	2.2111	6.7400	14.1934	0.0062	0.1593
	PIDn	16.3444	1.9109	6.0199	132.7099	0.0065	0.1433
	PD(1+PI)	19.1729	2.1999	6.8999	147.2990	0.0065	0.1627
	FOPI–FOPD	**6.8301**	**1.1009**	**3.3550**	**83.4001**	**0.0057**	**0.0787**
0.75 $\boldsymbol{\Delta P_{ESS}^{\max,ini}}$	FOPID	87.9129	25.3989	17.8500	490.5500	0.0101	0.4261
	PIDn	17.5879	2.1090	5.8809	121.7490	0.0074	0.1397
	PD(1+PI)	20.2560	2.1001	6.8890	141.6500	0.0071	0.1636
	FOPI–FOPD	**8.9046**	**1.2900**	**4.1023**	**84.6789**	**0.0054**	**0.0968**
1.25 $\boldsymbol{\Delta P_{ESS}^{\max,ini}}$	FOPID	48.6760	1.1670	13.5299	334.8700	0.0111	0.3326
	PIDn	15.9990	1.7980	5.8100	122.1209	0.0071	0.1380
	PD(1+PI)	18.9880	2.0200	6.6300	134.6890	0.0072	0.1578
	FOPI–FOPD	**10.9590**	**2.0002**	**4.5099**	**103.2599**	**0.0071**	**0.1067**

member is selected and checked to see if it follows the rules below in relation to all other agents in the population:

$$\begin{aligned} &obj_1\left[i\right] < obj_1\left[j\right]\ and \\ &obj_2\left[i\right] < obj_2\left[j\right],\ i \neq j \end{aligned} \tag{17}$$

After calculating Pareto optimal solutions, a suitable decision maker must choose the best compromise solution based on application priority. Fig. 5 illustrates the membership functions of the fuzzy objective functions, which are used to evaluate and select the optimal solution from the Pareto front. For each objective function f_i, a linear membership function is defined:

$$\mu_i = \begin{cases} \left(f_i^{\max} - f_i\right) / \left(f_i^{\max} - f_i^{\min}\right) & f_i^{\max} > f_i > f_i^{\min} \\ 1 & f_i^{\min} \geq f_i \\ 0 & f_i \geq f_i^{\max} \end{cases} \tag{18}$$

Index i represents the $i-th$ objective function in this equation. Objective functions can be normalized for non-dominated responses. So, for the $k-th$ non-dominated response the fuzzy decision-making (FDM^k) can be expressed as below:

$$FDM^k = \frac{\sum\limits_{i=1}^{2} \mu_i^k}{\sum\limits_{j=1}^{M} \sum\limits_{i=1}^{2} \mu_i^j} \tag{19}$$

Therefore, the best response is the one with the highest FDM^k value. The number of undefeated responses is M in Eq. (19).

5. NUMERICAL STUDIES

The system being analyzed is developed in the Simulink MATLAB 2020b environment. The NTVAC-MOPSO algorithm has identified the optimal controller coefficient values after 100

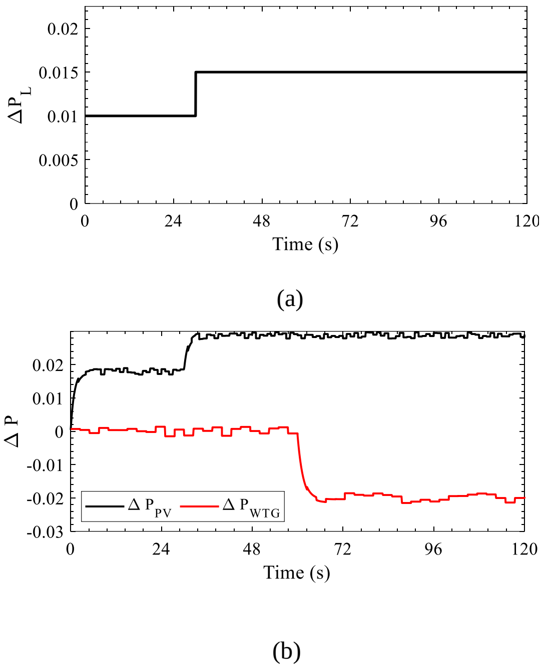

(a)

(b)

Fig. 11. Load disturbance and RESs' fluctuations in scenario 2 (p.u), (a) load disturbance, (b) output fluctuations of wind and solar units.

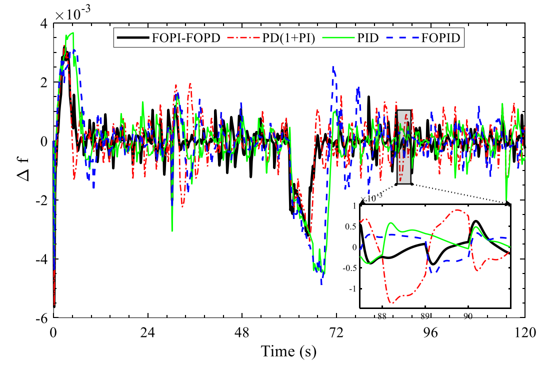

(a)

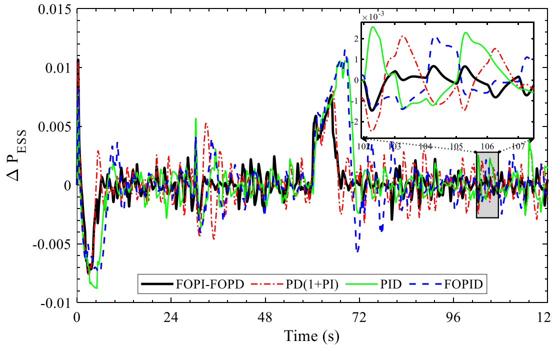

(b)

Fig. 12. Dynamic response of the system in scenario 2. (a) System frequency fluctuations (Hz), (b) Output variations of responsive loads (p.u). Solid line: FOPI–FOPD, dashed line: PID, dotted line: PD(1+PI) and dashed line: FOPID.

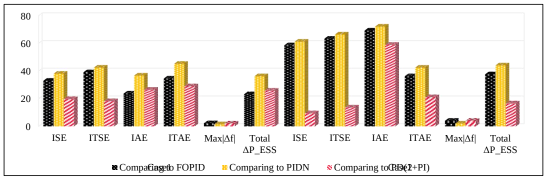

Fig. 13. Values of evaluation indicators in the first and second scenarios.

iterations ($Iter_{max} = 100$) using a population of 35. A demand-side load disturbance of magnitude 0.1 p.u. is introduced to the closed-loop system at $t = 1$ s, with a total simulation duration of 100 s ($t_{sim} = 100$ s). Given that the time variable is utilized in obj_1, introducing any perturbation within the time interval of 0 to 1 second may subject the controller to significant initial deviations. Consequently, it is prudent to introduce the disturbances after 1 second for the controller design. The FOMCON plugin in MATLAB is employed to model the FO operators, with the frequency range established between 10,000 and 0.001 [40]. Fig. 6 illustrates the block diagram of the studied μG, including the dynamic models of its components and the proposed control structure. The diagram also demonstrates the parameter tuning process using the employed optimization algorithm.

A comparison of the proposed controller with those employed in recent studies would be beneficial to assess its efficacy (i.e., the ability to produce the desired outcome) in ensuring μG frequency stability. A cascade PD(1+PI) controller, a classical PID controller with a derivative filter, and a fractional order controller (FOPID) have been developed and optimized for the LFC of the μG [39, 40]. The optimal values of the controller coefficients after optimization by NTVAC-MOPSO are presented in Table 1, while the Pareto front related to each controller's optimization is illustrated in Fig. 7. While Fig. 7 shows that the final objective function values for the FOPI-FOPD and PID(1+ID) controllers appear close, it is important to note that this plot primarily illustrates the convergence behavior of the optimization algorithm. The key advantage of the proposed FOPI-FOPD controller becomes evident under various operational scenarios, such as sudden load changes, uncertainties in RESs, and parametric variations, as detailed in Sections 5.1 to 5.4. To facilitate numerical comparison, the time domain evaluation indices ISE, ITSE, IAE, and ITAE are computed and documented for each scenario. The formulas for these indices are provided in Eqs. (20)–(23).

$$ITSE = \int_0^{t_{sim}} \left(\Delta {f_1}^2 + \Delta {f_2}^2\right) t\, dt + \int_0^{t_{sim}} P_{tie12}^2 t\, dt \tag{20}$$

$$ISE = \int_0^{t_{sim}} \left(\Delta {f_1}^2 + \Delta {f_2}^2\right) dt + \int_0^{t_{sim}} P_{tie12}^2\, dt \tag{21}$$

$$IAE = \int_0^{t_{sim}} |\Delta f|\, dt \tag{22}$$

$$ITAE = \int_0^{t_{sim}} t.\,|\Delta f|\, dt \tag{23}$$

Understanding these margins helps system designers assess power system vulnerability before instability. Modeling approximations, stochastic disturbances, and system load fluctuations can cause significant uncertainty. System performance is also evaluated using the frequency domain method. The system's relative stability is revealed by the Bode stability criterion. The gain margin (GM) shows the system's absolute stability and ability to oscillate peacefully during disturbances. The phase margin (PM) is the phase quantity that can be changed without destabilizing the system. Fig. 8 presents the Bode plots of the closed-loop system for various controllers, illustrating their frequency-domain response characteristics. The plots were generated using MATLAB and the Simulink Linear Analysis Tool. The system was modeled in

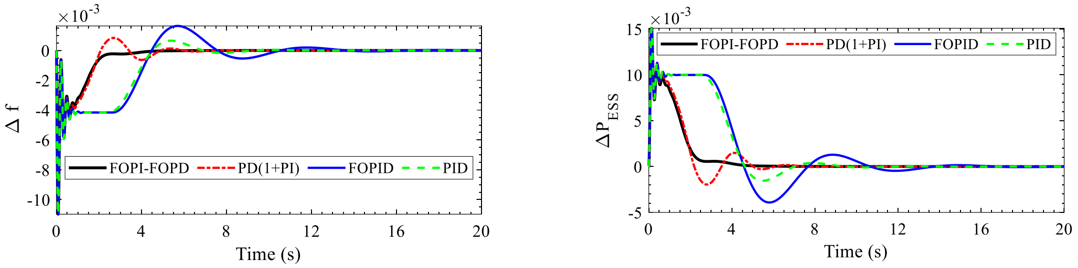

(*a*) (*b*)

Fig. 14. Dynamic response of the system in scenario 3 (D=1.25D_0, H=2.0H_0). (a system frequency fluctuations (Hz), (b) output changes of BESS and FESS storages (p.u). D=0.25D_0, H=0.25H_0.

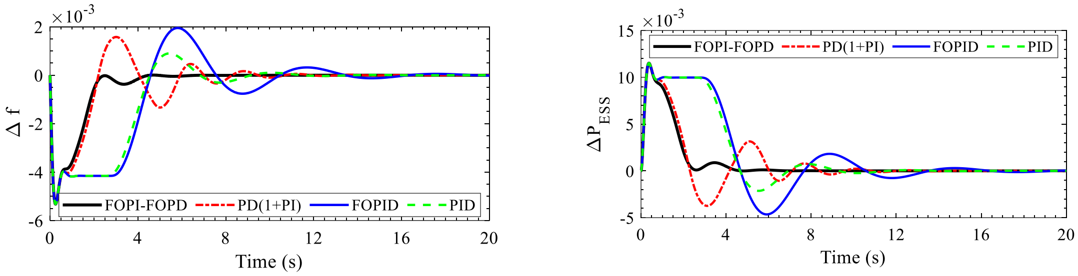

(*a*) (*b*)

Fig. 15. Dynamic response of the system in scenario 3 (D=1.25D_0, H=2.0H_0). (a) System frequency fluctuations, (b) Output changes of BESS and FC storages. D=0. 5D_0, H=1.5H_0.

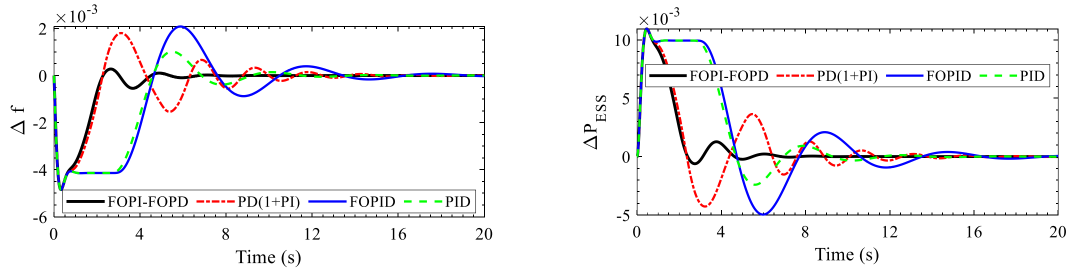

(*a*) (*b*)

Fig. 16. Dynamic response of the system in scenario 3 (D=1.25D_0, H=2.0H_0). (a) system frequency fluctuations (Hz), (b) output changes of BESS and FC storages (p.u).

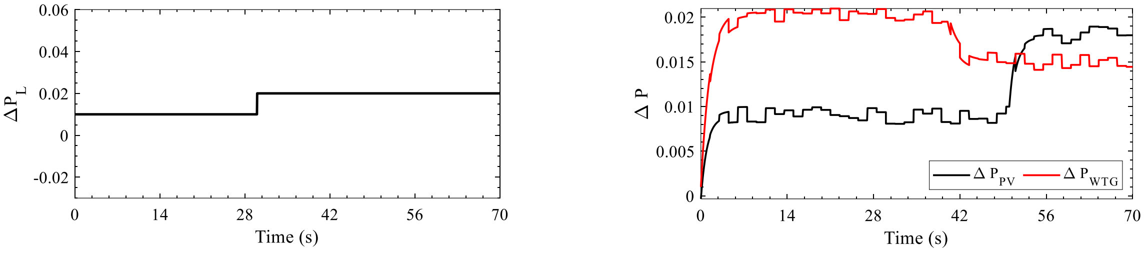

(*a*) (*b*)

Fig. 17. System disturbances in scenario 4 (p.u). (a) RESs' fluctuations, (b) demand-side disturbances.

Simulink with the proposed and comparative controllers, linearized around its operating point, and used to generate the Bode plots. These plots provide insights into the system's stability and frequency response. Table 2 shows PM and GM values. Positive PM and GM for a linear system indicate asymptotic stability. The PM is infinite for the specified controller, indicating that the closed-loop system can withstand long delays and ambiguous uncertainties without becoming unstable.

Various scenarios are used to assess the system's dynamic behavior. The operating conditions of the system in these scenarios are presented in Table 3.

5.1. Scenario 1: Sudden load change in a situation where the μG has a time delay

Controlling systems encounter complex challenges due to factors like time delays resulting from communication system congestion

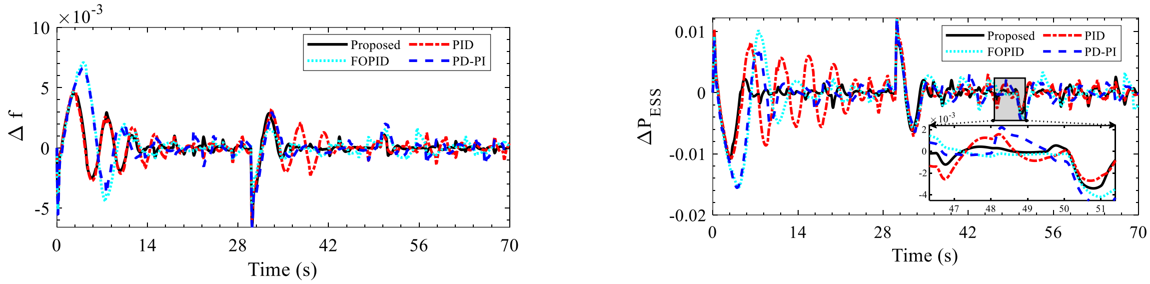

(a)

(b)

Fig. 18. Dynamic response of the system in scenario 4 where $\Delta P_{ESS}^{\max} = 0.5\Delta P_{ESS}^{\max,\ ini}$. (a) system frequency fluctuations (Hz), (b) output changes of BESS and FC storages (p.u).

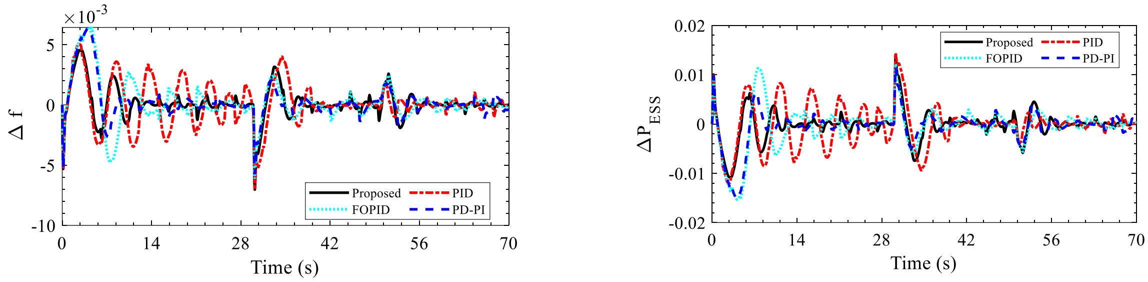

(a)

(b)

Fig. 19. Dynamic response of the system in scenario 4 where $\Delta P_{ESS}^{\max} = 0.75\Delta P_{ESS}^{\max,\ ini}$. (a) system frequency fluctuations (Hz), (b) output changes of BESS and FC storages (p.u).

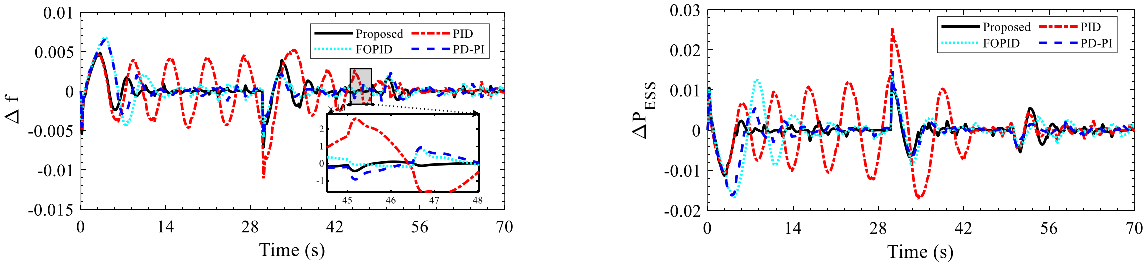

(a)

(b)

Fig. 20. Dynamic response of the system in scenario 4 where $\Delta P_{ESS}^{\max} = 1.25\Delta P_{ESS}^{\max,\ ini}$. (a) system frequency fluctuations (Hz), (b) output changes of BESS and FC storages (p.u).

or packet loss. The excitation signal of the control system is presumed to have a delay of 20 milliseconds. If the system frequency is 50 Hz, the delay between the control signal and the actual signal corresponds to one cycle. The load disturbances imposed on the demand side are illustrated in Fig. 9. Fig. 10 illustrates the system's dynamic response and the variations in the output power of the ESS set. The values of the time-based evaluation indices pertaining to the system's dynamic response are presented in Table 4. This table demonstrates that the proposed controller diminishes the total output power fluctuations of BESS and FC by 51%, 72%, and 80% in comparison to the PD(1+PI), FOPID, and PIDn controllers, respectively. Consequently, the proposed controller demonstrates superior performance, evidenced by its expedited error recovery speed, reduced maximum frequency deviation, and diminished reliance on the capacity of the ESSs.

5.2. Scenario 2: RESs' uncertainties

The output power of RES-based generation units is contingent upon weather conditions and possesses inherent uncertainties, which consequently influence system dynamics. In Scenario 2, the uncertainties associated with RESs and demand are modeled by applying variations in the input power of the corresponding RES units. These variations are designed to simulate real-world fluctuations, such as changes in wind speed for wind turbines or solar irradiance for photovoltaic units. Additionally, probabilistic input signals with a normal distribution are introduced to represent the stochastic behavior of RESs and demand. This approach ensures that the proposed controller is tested under realistic and challenging conditions, demonstrating its robustness and adaptability. The system load variations ΔP_L over 120 seconds are depicted in Fig. 11-(a), while the output power fluctuations of renewable energy source-based units (ΔP_{WTG} and ΔP_{PV}) are illustrated in Fig. 11-(b). Under these conditions, the system's dynamic behavior, encompassing frequency fluctuations Δf and variations in the ESS contribution ΔP_{ESS}, is illustrated in Fig. 12. Table 5 presents the time domain indices under various controllers. The frequency deviation observed in this scenario by the other controllers is at least threefold greater than that attained by the proposed FOPI–FOPD controller, which is realized by the PD(1+PI) controller. In the interim, the PD(1+PI) controller has utilized nearly double the capacity of Energy Storage Systems compared to the proposed controller. Fig. 13 illustrates the enhancement of evaluation indices in the first and second scenarios when employing the FOPI–FOPD controller as opposed to alternative controllers.

5.3. Scenario 3: Parametric uncertainties in the system model

Numerous studies indicate that even the most advanced mathematical models fail to accurately depict the dynamics of real systems. Consequently, the control mechanism must accommodate the discrepancies between actual system values and their mathematical representations. In this investigation, the inertia (H) and damping coefficient (D) parameters in the system model are examined under two conditions distinct from the initial parameters for which the controllers were designed (i.e., D_0 and H_0). A load disturbance ΔP_L=0.01 p.u is applied to the system at t=0 s, with a presumed time delay of $\tau = 40$ ms in the transmission of the control signal. The resistance and response of the controllers are illustrated in Figs. 14–16, alongside with the impact of each scenario on the variation of output power from the ESSs (ΔP_{ESS}). Key time domain evaluation metrics are summarized in Table 6 to facilitate a comparison of controller performance.

The FOPI–FOPD's low ITAE values in all scenarios highlight its capability to recover from disturbances faster and more efficiently than the other controllers. The FOPI–FOPD controller minimizes energy storage system (ESS) usage across all scenarios. For example: $D = 0.25D_0$, $H = 0.25H_0$, it achieves a Total ΔP_{ESS} of 0.0162, which is 14% lower than the FOPID and approximately 59% lower than the PIDn. Moreover, As the system parameters change (i.e., different combinations of D and H) the FOPI–FOPD controller demonstrates consistent performance across all indices, maintaining its superiority over the other controllers.

5.4. Scenario 4: Investigating the ESSs' participation impact on the $\mu G's$ dynamic behavior

This scenario assesses the maximum contribution of BESS and FC storage devices, denoted as ΔP_{ESS}^{max}, within the LFC control loop. Relying on the storage capacity of devices to ensure system stability is undesirable, despite their potential for rapid response. The control mechanism must be autonomous, operate within acceptable limits, and maintain system stability independently. Consequently, in this context, the pertinent assessments are conducted by altering the cap on the contribution of storage devices, which was deemed equivalent to 0.51 during the design phase. In this context, ΔP_{ESS}^{max} is evaluated at half, three-quarters, and 1.25 times the initial value ($\Delta P_{ESS}^{max,ini}$), and the system's dynamic behavior is analyzed.

Load disturbances and RESs are integrated into the system as illustrated in Fig. 17. Figs. 18, 19, and 20 illustrate the system's dynamic behavior, while Table 7 presents the time domain evaluation indices.

Unlike other controllers, which may excel in one or two performance indices, the FOPI–FOPD achieves a balanced performance across all metrics, highlighting its suitability as a comprehensive solution for load-frequency control. The Total ΔP_{ESS}s values highlight that the FOPI–FOPD controller requires the least energy contribution from the ESS, which is crucial for reducing wear and extending the lifespan of storage systems. At 0.5 $\Delta P_{ESS}^{max,ini}$, its ESS participation is 0.0787, less than half of FOPID (0.1593) and lower than PIDn (0.1433) and PD(1+PI) (0.1627). The FOPI–FOPD controller demonstrates exceptional adaptability across varying levels of ESS participation, consistently outperforming other methods under all scenarios. This robustness ensures effective load-frequency stabilization regardless of the ESS contribution.

6. CONCLUSION

This study presented a novel FOPI–FOPD controller for the LFC in islanded μG, addressing the challenges posed by system uncertainties, RESs integration, and ESSs dynamics. By employing MOPSO-NTVAC and fuzzy decision-making, the controller was designed to deliver superior performance across a range of operational scenarios. The evaluations focused on key performance indices, including error minimization, frequency stability, and efficient energy storage utilization, comparing the proposed controller with other control methods to assess its effectiveness comprehensively.

The comparative analysis confirms that the FOPI–FOPD controller consistently outperforms controllers such as FOPID, PIDn, and PD(1+PI) across various performance metrics, including error indices, frequency deviation control, and ESS utilization. Its ability to minimize total ESS participation and maintain stability under different scenarios demonstrates its robustness and adaptability for real-world applications. These results highlight the proposed controller's potential to enhance μG resilience and efficiency, offering a reliable solution for advanced load-frequency control in modern power systems.

Acknowledgments

This work has been financially supported by the research deputy of University of Mohaghegh Ardabili. The grant No. was 1401.d.9.14322.

REFERENCES

[1] J. Heidary, M. Gheisarnejad, H. Rastegar, and M. H. Khooban, "Survey on microgrids frequency regulation: Modeling and control systems," *Electr. Power Syst. Res.*, vol. 213, p. 108719, 2022.

[2] G. Zhang, H. Zhong, Z. Tan, T. Cheng, Q. Xia, and C. Kang, "Texas electric power crisis of 2021 warns of a new blackout mechanism," *CSEE J. Power Energy Syst.*, vol. 8, no. 1, pp. 1–9, 2022.

[3] M. N. H. Shazon, A. Jawad, *et al.*, "Frequency control challenges and potential countermeasures in future low-inertia power systems: A review," *Energy Rep.*, vol. 8, pp. 6191–6219, 2022.

[4] A. Alahmad, A. Saffarian, S. G. Seifossadat, and S. S. Mortazavi, "Frequency and voltage stability of the islanded microgrid with multi dc-bus based-inverter using droop control," *J. Oper. Autom. Power Eng.*, vol. 13, no. 2, pp. 121–126, 2025.

[5] H. Shayeghi and A. Rahnama, "Multistage pd-(1+ pi) controller design for frequency control of a microgrid considering demand response program," in *Smart Grid 3.0: Comput. Commun. Technol.*, pp. 241–274, Springer, 2023.

[6] A. Latif, S. S. Hussain, D. C. Das, T. S. Ustun, and A. Iqbal, "A review on fractional order (fo) controllers' optimization for load frequency stabilization in power networks," *Energy Rep.*, vol. 7, pp. 4009–4021, 2021.

[7] V. P. Singh, N. Kishor, P. Samuel, and S. R. Mohanty, "Impact of communication delay on frequency regulation in hybrid power system using optimized h-infinity controller," *IETE J. Res.*, vol. 62, no. 3, pp. 356–367, 2016.

[8] Y. Rao, J. Yang, J. Xiao, B. Xu, W. Liu, and Y. Li, "A frequency control strategy for multimicrogrids with v2g based on the improved robust model predictive control," *Energy*, vol. 222, p. 119963, 2021.

[9] A. Abazari, M. M. Soleymani, M. Babaei, M. Ghafouri, H. Monsef, and M. T. Beheshti, "High penetrated renewable energy sources-based aompc for microgrid's frequency regulation during weather changes, time-varying parameters and generation unit collapse," *IET Gener. Trans. Distrib.*, vol. 14, no. 22, pp. 5164–5182, 2020.

[10] Y. Mi, X. He, X. Hao, Z. Li, Y. Fu, C. Wang, and J. Wang, “Frequency control strategy of multi-area hybrid power system based on frequency division and sliding mode algorithm,” *IET Gener. Transm. Distrib.*, vol. 13, no. 7, pp. 1145–1152, 2019.

[11] K. Liao and Y. Xu, “A robust load frequency control scheme for power systems based on second-order sliding mode and extended disturbance observer,” *IEEE Trans. Ind. Inf.*, vol. 14, no. 7, pp. 3076–3086, 2017.

[12] Y. Arya, “Effect of electric vehicles on load frequency control in interconnected thermal and hydrothermal power systems utilising cf-foidf controller,” *Gener. Transm. Distrib.*, vol. 14, no. 14, pp. 2666–2675, 2020.

[13] S. Padhy and S. Panda, “Application of a simplified grey wolf optimization technique for adaptive fuzzy pid controller design for frequency regulation of a distributed power generation system,” *Prot. Control Mod. Power Syst.*, vol. 6, no. 1, pp. 1–16, 2021.

[14] H. Shayeghi, A. Rahnama, and N. Bizon, “Green microgrid’s lfc using recursive step-by-step optimized multi-stage fuzzy controller with separated inference systems,” *Renewable Energy Focus*, vol. 51, p. 100625, 2024.

[15] A. Younesi, H. Shayeghi, and P. Siano, “Assessing the use of reinforcement learning for integrated voltage/frequency control in ac microgrids,” *Energies*, vol. 13, no. 5, p. 1250, 2020.

[16] K. Peddakapu, M. Mohamed, P. Srinivasarao, Y. Arya, P. Leung, and D. Kishore, “A state-of-the-art review on modern and future developments of agc/lfc of conventional and renewable energy-based power systems,” *Renewable Energy Focus*, vol. 43, pp. 146–171, 2022.

[17] N. Hakimuddin, I. Nasiruddin, T. S. Bhatti, and Y. Arya, “Optimal automatic generation control with hydro, thermal, gas, and wind power plants in 2-area interconnected power system,” *Electr. Power Compon. Syst.*, vol. 48, no. 6-7, pp. 558–571, 2020.

[18] Y. Arya, N. Kumar, P. Dahiya, G. Sharma, E. Çelik, S. Dhundhara, and M. Sharma, “Cascade-iλdμn controller design for agc of thermal and hydro-thermal power systems integrated with renewable energy sources,” *IET Renewable Power Gener.*, vol. 15, no. 3, pp. 504–520, 2021.

[19] K. Peddakapu, P. Srinivasarao, M. Mohamed, Y. Arya, and D. K. Kishore, “Stabilization of frequency in multi-microgrid system using barnacle mating optimizer-based cascade controllers,” *Sustainable Energy Technol. Assess.*, vol. 54, p. 102823, 2022.

[20] R. K. Khadanga, S. Padhy, S. Panda, and A. Kumar, “Design and analysis of multi-stage pid controller for frequency control in an islanded micro-grid using a novel hybrid whale optimization-pattern search algorithm,” *Int. J. Numer. Modell. Electron. Networks Devices Fields*, vol. 31, no. 5, p. e2349, 2018.

[21] H. Shayeghi, A. Rahnama, N. Takorabet, P. Thounthong, and N. Bizon, “Designing a multi-stage pd (1+ pi) controller for dc–dc buck converter,” *Energy Rep.*, vol. 8, pp. 765–773, 2022.

[22] E. Çelik, N. Öztürk, Y. Arya, and C. Ocak, “(1+ pd)-pid cascade controller design for performance betterment of load frequency control in diverse electric power systems,” *Neural Comput. Appl.*, vol. 33, no. 22, pp. 15433–15456, 2021.

[23] H. Shayeghi and A. Rahnama, “Frequency regulation of a standalone interconnected ac microgrid using innovative multistage tdf (1+ fopi) controller,” *J. Oper. Autom. Power Eng.*, vol. 12, no. 2, pp. 121–133, 2024.

[24] K. Singh and Y. Arya, “Jaya-itdf control strategy-based frequency regulation of multi-microgrid utilizing energy stored in high-voltage direct current-link capacitors,” *Soft Comput.*, vol. 27, no. 9, pp. 5951–5970, 2023.

[25] H. Shayeghi, A. Rahnama, and N. Bizon, “Tfodn-fopi multi-stage controller design to maintain an islanded microgrid load-frequency balance considering responsive loads support,” *IET Gener. Transm. Distrib.*, vol. 17, no. 14, pp. 3266–3285, 2023.

[26] H. S. A. Rahnama, “Designing a pd-(1+ pi) controller for lfc of an entirely renewable microgrid using pso-tvac,” *Int. J. “Tech. Phys. Probl. Eng.”*, vol. 12, no. 45, pp. 19–27, 2020.

[27] A. Latif, S. S. Hussain, D. C. Das, and T. S. Ustun, “Optimization of two-stage ipd-(1+ i) controllers for frequency regulation of sustainable energy based hybrid microgrid network,” *Electron.*, vol. 10, no. 8, p. 919, 2021.

[28] D. K. Gupta, A. K. Soni, A. V. Jha, S. K. Mishra, B. Appasani, A. Srinivasulu, N. Bizon, and P. Thounthong, “Hybrid gravitational–firefly algorithm-based load frequency control for hydrothermal two-area system,” *Math.*, vol. 9, no. 7, p. 712, 2021.

[29] D. K. Gupta, A. V. Jha, B. Appasani, A. Srinivasulu, N. Bizon, and P. Thounthong, “Load frequency control using hybrid intelligent optimization technique for multi-source power systems,” *Energies*, vol. 14, no. 6, p. 1581, 2021.

[30] S. Nojavan and K. Zare, *Demand response application in smart grid*. Springer, 2020.

[31] A. A. Rafia and R. Jayaprakash, “Fractional order controller for power control in ac islanded pv microgrid using electric vehicles,” *Recent Adv. Electr. Electron. Eng.*, vol. 17, no. 2, pp. 137–146, 2024.

[32] A. Al-Hinai, H. Alyammahi, and H. H. Alhelou, “Coordinated intelligent frequency control incorporating battery energy storage system, minimum variable contribution of demand response, and variable load damping coefficient in isolated power systems,” *Energy Rep.*, vol. 7, pp. 8030–8041, 2021.

[33] F. R. Badal, P. Das, S. K. Sarker, and S. K. Das, “A survey on control issues in renewable energy integration and microgrid,” *Prot. Control Mod. Power Syst.*, vol. 4, no. 1, pp. 1–27, 2019.

[34] R. Dadi, K. Meenakshy, and S. Damodaran, “A review on secondary control methods in dc microgrid,” *J. Oper. Autom. Power Eng.*, vol. 11, no. 2, pp. 105–112, 2023.

[35] M. Gheisarnejad and M. H. Khooban, “Secondary load frequency control for multi-microgrids: Hil real-time simulation,” *Soft Comput.*, vol. 23, pp. 5785–5798, 2019.

[36] J. Heidary and H. Rastegar, “A novel computational technique using coefficient diagram method for load frequency control in an interconnected power system,” *J. Electr. Syst. Inf. Technol.*, vol. 9, no. 1, p. 22, 2022.

[37] J. Morsali, K. Zare, and M. T. Hagh, “Comparative performance evaluation of fractional order controllers in lfc of two-area diverse-unit power system with considering gdb and grc effects,” *J. Electr. Syst. Inf. Technol.*, vol. 5, no. 3, pp. 708–722, 2018.

[38] R. Alayi, F. Zishan, S. R. Seyednouri, R. Kumar, M. H. Ahmadi, and M. Sharifpur, “Optimal load frequency control of island microgrids via a pid controller in the presence of wind turbine and pv,” *Sustainability*, vol. 13, no. 19, p. 10728, 2021.

[39] S. Dhundhara, M. Sharma, F. Guéniat, and Y. Arya, “Overview of the renewable-dominated power systems and their frequency regulation issues,” in *Adv. Freq. Regul. Strategies Renewable-Dominated Power Syst.*, pp. 1–19, Elsevier, 2024.

[40] A. Tepljakov and A. Tepljakov, “Fomcon: fractional-order modeling and control toolbox,” *Fract.-Order Model. Control Dyn. Syst.*, pp. 107–129, 2017.